On the Convergence of DGFEM Applied to the Discrete Ordinates Transport Equation for Structured and Unstructured Triangular Meshes

Yaqi Wang and Jean C. Ragusa*

Texas A&M University
Department of Nuclear Engineering
College Station, Texas 77843

Abstract — *The convergence properties of the discontinuous Galerkin finite element method (DGFEM) applied to the transport equation are presented for variants of Larsen's test case. The analysis is performed for two-dimensional structured and unstructured triangular meshes, with DGFEM approximations up to order 4. Pure absorber media and scattering media are considered. The influence of the mesh alignment with the singularities of the transport solution is described. The numerically observed convergence rates are related to theoretical results.*

I. INTRODUCTION

The convergence of various spatial discretizations of the discrete ordinates transport equations has been the focus of many papers for more than four decades. Earlier work mostly dealt with finite difference approximations (diamond differences, weighted diamond differences) (see, for instance, Refs. 1 through 5). In Refs. 1 and 2, Madsen established the stability and second-order convergence of a class of finite difference approximations (the diamond difference method of Carlson and weighted central differences) in an L_2 discrete norm. Madsen's proof required that the exact solution possess bounded third partial derivatives.[1] As noted by Arkuszewski, Kulikowska, and Mika[6] and Larsen,[7] such conditions are seldom verified in realistic problems, where singular characteristics are present. This triggered several numerical studies of the convergence of finite difference schemes, typically in simple one-dimensional (1-D) or two-dimensional (2-D) configurations; see, for instance, Refs. 7 and 8. Larsen provided convergence rates of the numerical solutions in L_1, L_2, and L_∞ norms for various mesh refinements. In the 1-D case,[8] these rates, measured in any norm, showed second-order convergence,

whereas in the 2-D case, the rates depended on the norm utilized and were fractional powers of the mesh size. More recently, Duo and Azmy[9] numerically investigated the convergence rates of weighted diamond difference, nodal, and characteristics methods, using a variation of the test case proposed earlier by Larsen. The nodal and characteristics methods tested included constant, linear, and quadratic spatial approximations.

In this paper, we study the convergence properties of another widely used spatial discretization technique for transport, namely, the discontinuous finite element technique. The discontinuous Galerkin (DG) finite element method (DGFEM), originally derived for discrete ordinates neutron transport in the early 1970s, is another technique commonly used to spatially discretize the transport equation. The DGFEM is a versatile method, well suited for unstructured meshes and adaptive mesh refinement (AMR), and has enjoyed many theoretical and applied developments. For instance, linear DGFEM has been used for the numerical solution of the discrete ordinates transport equation on unstructured tetrahedral meshes[10,11] and hexahedral meshes.[10] Ragusa and Wang[12] and Wang, Ragusa, and DeHart[13] implemented a higher-order DGFEM for unstructured triangular meshes. In other disciplines, where hyperbolic conservation laws are commonly present, e.g., fluid dynamics, linear and

---

*E-mail: ragusa@ne.tamu.edu

higher-order DGFEMs are well established, appearing in mathematics textbooks.[14–16] Theoretical aspects have also significantly progressed since the inception of the method, and later in the paper we briefly recall some of the convergence results. This paper summarizes our analysis of the convergence properties of the DGFEM applied to neutron transport for various orders of spatial approximation (from $p = 1$ to $p = 4$), and we compare the observed numerical rates with theoretical results.

The outline of the paper is as follows. In Sec. II, we present the DGFEM applied to the one-group discrete ordinates transport equations and introduce the polynomial representation used. In Sec. III, we review the existing convergence results and discuss the expected orders of convergence. In Sec. IV, we present the procedure utilized to compute the L_2 norm of the error. Results are given in Sec. V, where we consider problems similar to the ones used by Larsen and Azmy, namely, a single-ordinate incident flux on a homogeneous domain. The cases of scattering and no scattering (pure absorber) are analyzed; boundary conditions (incident fluxes) will be imposed on either a single face (left incidence), or on adjacent faces (both left and bottom incidences), providing examples where the exact transport solution is either continuous or discontinuous. The mesh topology (alignment or not with the singular characteristics) is also accounted for in our discussions. Concluding remarks are given in Sec. VI.

II. DISCONTINUOUS GALERKIN FORMULATION

Historically, the DGFEM was introduced by Reed and Hill[18] and Reed et al.[19] for solving the linear discrete ordinates (S_N) neutron transport equation. Soon thereafter, the first mathematical analysis was published by Lesaint and Raviart.[20] The method is described below for the one-group case with isotropic scattering and source. The one-speed steady-state neutron transport equation in a domain D with boundary ∂D is given by

$$\vec{\Omega} \cdot \vec{\nabla} \Psi(\vec{r}, \vec{\Omega}) + \sigma(\vec{r}) \Psi(\vec{r}, \vec{\Omega})$$

$$= \frac{\sigma_{s,0}(\vec{r}) \Phi(\vec{r}) + Q(\vec{r})}{4\pi} = q(\vec{r}) \quad \text{on } D \quad (1)$$

and

$$\Psi(\vec{r}_b, \vec{\Omega}) = \Psi^{inc}(\vec{r}_b, \vec{\Omega})$$

$$\text{on } \partial D^- = \{(\vec{r}_b \in \partial D), \vec{\Omega} \cdot \vec{n} < 0\} \ , \quad (2)$$

where

$$\Psi(\vec{r}, \vec{\Omega}) = \text{angular flux at position } \vec{r} \text{ in direction } \vec{\Omega}$$

$$Q = \text{isotropic extraneous source term}$$

$$\sigma, \sigma_{s,0} = \text{total and isotropic scattering macroscopic cross sections, respectively } (Q, \sigma, \text{ and } \sigma_{s,0} \text{ are assumed to be piecewise constant})$$

$$D = \text{spatial domain}$$

$$\partial D = \text{spatial domain boundary.}$$

The scalar flux Φ is defined by

$$\Phi(\vec{r}) = \int_{4\pi} d\Omega \, \Psi(\vec{r}, \vec{\Omega}) \xrightarrow[\text{discrete ordinates}]{} \sum_{d=1}^{d=N_d} w_d \Psi(\vec{r}, \vec{\Omega}_d) \ .$$

(3)

In the S_N (discrete ordinates) method, the transport equation [Eq. (1)] is solved along discrete directions $\vec{\Omega}_d$ belonging to a given angular quadrature set $\{\vec{\Omega}_d, w_d\}_{1 \le d \le N_d}$, and the integral yielding the scalar flux is replaced by the quadrature formula, as shown in Eq. (3). We employ the standard source iteration (SI) method to solve the S_N equations: A previous iteration of the scalar flux is used to compute the right-side total source term q; then, the transport equation is solved for each direction $\vec{\Omega}_d$ (a process typically referred to as a transport sweep), yielding new values for the angular fluxes Ψ_d, which are used to compute a new value of the scalar flux [Eq. (3)]. For more details on the S_N method and its iterative solution using SI, please refer to Ref. 21. For the examples considered here (a pure absorber and a mild scatterer), SI converges very effectively. We use a convergence tolerance of 10^{-12} for SI, thus ensuring that virtually no iteration error is present.

For notational simplicity, we let $\Psi_d(\vec{r}) = \Psi(\vec{r}, \vec{\Omega}_d)$ and omit the direction subscript d whenever unnecessary. A mesh T_h is used to discretize the domain D into elements K (specifically triangles in our application), such that the union of all the elements fully covers D, i.e., $\bigcup_{K \in T_h} K = D$. We also assume that the outer boundary of D consists of straight segments.

We now introduce the volume and surface integrals on any element K and its boundary ∂K, respectively, as follows:

$$(f, g)_K = \int_K d^3 r f(r) g(r) \quad (4)$$

and

$$(f, g)_{\partial K} = \int_{\partial K} d^2 r |\vec{\Omega} \cdot \vec{n}| f(r) g(r) \ . \quad (5)$$

In the case of 2-D geometries, these definitions are to be understood as surface and edge integrals. The DGFEM applied to Eq. (1) is obtained by multiplying Eq. (1) by a (discontinuous) test function b_i ($i = 1, \ldots$, total number of spatial unknowns) and integrating the result over each element, i.e.,

$$\sum_{K \in T_h} \{-(\vec{\Omega} \cdot \vec{\nabla} b_i, \Psi)_K + (b_i, \sigma \Psi)_K + (\Psi^+, b_i^+)_{\partial K^+}\}$$

$$= \sum_{K \in T_h} \{(q, b_i)_K + (\Psi^-, b_i^+)_{\partial K^-}\} , \qquad (6)$$

where

$\partial K^- =$ inflow boundary ($\partial K^- = \{x \in \partial K$ such that $\vec{\Omega} \cdot \vec{n} < 0\}$)

$\partial K^+ =$ outflow boundary ($\partial K^+ = \{x \in \partial K$ such that $\vec{\Omega} \cdot \vec{n} > 0\}$)

$f^+ =$ restriction of the function f taken from within the element K

$f^- =$ restriction of the function f taken from the neighboring element of K.

In the case of straight element boundaries, the quantity $\vec{\Omega} \cdot \vec{n}$ can be factored out of the boundary integrals. The left-side boundary integral in Eq. (6) contains the flux unknowns for each element K, whereas the right-side boundary integral contains the upwind values, i.e., the incoming contributions from the neighboring upwind elements. When an element lies on the domain boundary ∂D, the incoming contribution is given by Eq. (2).

We have implemented the DGFEM, with basis functions up to order 4. For any order p, we hereafter refer to the DGFEM implementation as DGFEM(p). For more details regarding high-order finite element basis functions, we refer the reader to Refs. 15, 16, and 17.

Our implementation uses 2-D structured and unstructured geometries, meshed with triangular elements. The unstructured meshes shown in Sec. V are generated with the triangle mesh generator.[22]

III. REVIEW OF THEORETICAL CONVERGENCE RESULTS

In the analysis of the DGFEM by Lesaint and Raviart in 1974, the convergence rate, measured in the $L_2(D)$ norm, was demonstrated to be of order p for an arbitrary triangulation of the domain and $p + 1$ for a rectangular Cartesian grid, where p represents the polynomial order of the spatial approximation.[20] This rate of p was suboptimal for general triangulations, and later, in 1983, Johnson and Pitkaranta[23] established that the convergence rate for the neutron transport equation, measured in any $L_q(D)$ norm, $q > 1$, thus including the $L_2(D)$ norm, can be $p + \frac{1}{2}$, depending on the smoothness of the exact solution, i.e.,

$$\|\Phi - \Phi_{exact}\|_{L_2(D)} \le Ch^{\min(p+1/2, r-1/2)} , \qquad (7)$$

where r is the regularity index of the exact solution. Peterson[24] numerically verified Johnson and Pitkaranta's optimum result using topologically irregular meshes.

Finally, Richter[25] showed that on topologically regular meshes, the result by Johnson and Pitkaranta can be improved by another half-integer value, yielding in such situations a convergence value for the DGFEM of

$$\|\Phi - \Phi_{exact}\|_{L_2(D)} \le Ch^{\min(p+1, r)} . \qquad (8)$$

This result by Richter, already demonstrated in the original paper of Lesaint and Raviart[20] but only for rectangles, is well known in the transport community as the second-order accuracy of the linear DGFEM ($p = 1$).

We note that all the above convergence estimates are limited by the regularity r of the solution. Under usual smoothness of the data, such as piecewise polynomial cross-section data and incoming flux values that coincide with the spatial mesh (that is, we exclude the case where the supplied data are discontinuous within an element), the exact transport solution belongs, at most, in the Hilbert space $H^{3/2-\varepsilon}(D)$ (Refs. 23 and 26), yielding a regularity coefficient of $r = \frac{3}{2} - \varepsilon$. The ε parameter is positive and extremely small, and for practical purposes the observed regularity is simply $\frac{3}{2}$. In the case of a pure absorber (or void), the exact transport solution can be discontinuous and is only found in the $H^{1/2-\varepsilon}(D)$ space, yielding a practical regularity index of $\frac{1}{2}$ (see Ref. 26 for more details on the fractional Sobolev spaces). From these theoretical results, it may seem that the regularity of the transport solution can be a grave impediment to high-order numerical techniques, but the regularity index will dictate the convergence rates only in the asymptotic range, i.e., usually only for very fine meshes that can be much smaller than meshes employed in practical computations. That is to say, we may enjoy higher convergence rates (up to order $p + 1$) in a preasymptotic range, before noticing the smaller regularity-constrained convergence rate. In Sec. V, we provide such examples and further discuss this point.

The convergence of DG methods has also been analyzed in another norm, the DG norm,[20,27,28] which contains the L_2 norm in the interior of an element [the standard L_2 norm, defined by the inner product Eq. (4)] and additional jump terms occurring at the interelement boundaries:

$$\|u\|_{DG}^2 = \sum_{K \in T_h} \left[\|u\|_{L_2(K)}^2 + \frac{1}{2} (u^+ - u^-, u^+ - u^-)_{\partial K} \right] .$$

$$\qquad (9)$$

Defining a norm on ∂K using the inner product of Eq. (5), we have

$$\|u\|_{DG}^2 = \sum_{K \in T_h} \left[\|u\|_{L_2(K)}^2 + \frac{1}{2} \|u^+ - u^-\|_{L_2(\partial K)}^2 \right] . \qquad (10)$$

In the DG norm, the theoretical convergence rates one can expect are

$$\|\Phi - \Phi_{exact}\|_{\mathrm{DG}} \le Ch^{\min(p+1/2,\, r-1/2)} \ , \qquad (11)$$

where we note that this is simply one-half integer less than the convergence rate measured in the standard L_2 norm. We also note that this convergence rate is due to the jump terms appearing in the DG norm (the L_2 volumetric term converges at the standard and higher L_2 rate). We also point out that for solutions belonging only in the $H^{1/2-\varepsilon}(D)$ space, the convergence rate measured in the DG norm should tend toward zero as the mesh is refined.

IV. ERROR COMPUTATION

In this section, we describe how the reference solution Φ_{ref} is obtained and explain the procedure used to compute the L_2 (and DG) norms of the error $\Phi - \Phi_{ref}$.

IV.A. Fine Numerical Solution Obtained Using Adaptive Mesh Refinement

For a pure absorbing medium, an analytical solution to the transport equation can be obtained. Because we will also consider cases with scattering, we have chosen to obtain an extremely precise numerical solution that will serve as the reference solution in the error norm calculations. Because obtaining a numerical reference solution using uniform mesh refinement is an extremely greedy process, the reference solution is obtained using an AMR procedure, which we describe below. In this AMR process, two numerical solutions are computed at each adaptivity cycle: a coarse solution and a fine solution. The difference between the two solutions is an accurate representation of the spatial error, which we employ to determine the next adapted mesh. We denote by Φ_h^0 the numerical solution on the given initial mesh T_h^0 and by $\Phi_{h/2}^0$ the numerical solution on a finer mesh $T_{h/2}^0$, where the finer mesh was obtained by subdividing every triangle in T_h^0 into four smaller triangles. The solution $\Phi_{h/2}^0$ is closer to the reference solution than is Φ_h^0, and we can write the difference between the two numerical solutions as

$$\Phi_h^0 - \Phi_{h/2}^0 = \Phi_h^0 - \Phi_{ref} - (\Phi_{h/2}^0 - \Phi_{ref})$$

$$= e_h^0 - e_{h/2}^0$$

$$\simeq e_h^0 \ , \qquad (12)$$

where e_h^0 and $e_{h/2}^0$ are the error in the meshes T_h^0 and $T_{h/2}^0$, respectively. Because $e_{h/2}^0$ is smaller than e_h^0 (in the fine mesh limit), the difference $\Phi_h^0 - \Phi_{h/2}^0$ is a good representation of the error on mesh T_h^0. Then, the elements of T_h^0 with the largest error are selected for refinement (i.e., subdivided into four smaller trian-
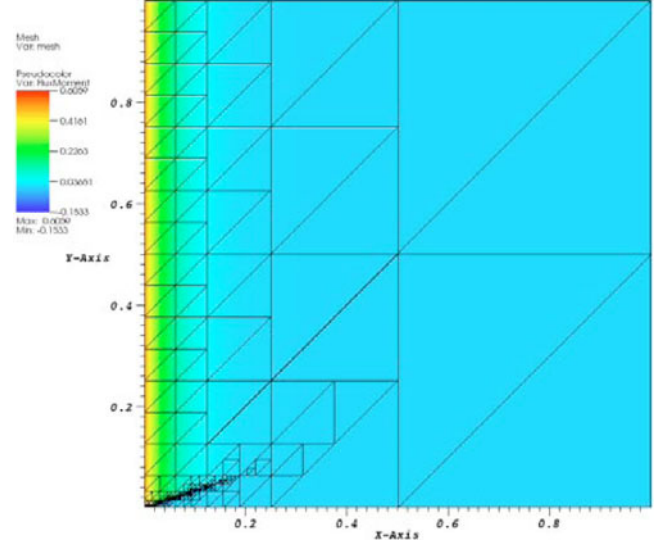

Fig. 1. Example of a reference solution, obtained using AMR (pure absorber case, 20-mfp domain, flux incident on the left face at ~18 deg).

gles), yielding a new mesh T_h^1. The process is then iterated by (a) creating the new finer mesh $T_{h/2}^1$ by uniform refinement of T_h^1, (b) computing Φ_h^1 on T_h^1 and $\Phi_{h/2}^1$ on $T_{h/2}^1$, (c) estimating the error $e_h^1 \simeq \Phi_h^1 - \Phi_{h/2}^1$ on T_h^1, and so on. We performed a total of 16 AMRs using the principle outlined above. The final numerical solution obtained using the AMR process, $\Phi_{h/2}^{15}$, serves as the reference solution in our error norm procedure. The uniform mesh refinement is used for the convergence studies. An example of an AMR reference solution (with its corresponding mesh) is shown in Fig. 1 in the case of an initially structured mesh T_h^0. In all our computations, the reference solution was obtained using DGFEM(4), i.e., with fourth-order polynomial bases. For clarity, we will refer to the final mesh from this AMR procedure as T^{AMR}. The reference AMR solution will be referred to as Φ_{ref} and will be used to measure the errors due solely to the spatial discretization. Angular discretization error is a separate topic and is not considered here.

IV.B. Calculation of the L_2 Norm of the Error on a Series of Embedded Meshes

By definition, the L_2 norm of the error on mesh T_h is

$$\|\Phi_h - \Phi_{ref}\|_{L_2(D)} = \sqrt{\int_D d^3 r (\Phi_h - \Phi_{ref})^2}$$

$$= \sqrt{\sum_{K \in T_h} \int_K d^3 r (\Phi_h - \Phi_{ref})^2} \ , \quad (13)$$

where the integral over the whole domain D has been divided into the elements K of the triangulation T_h on which Φ_h is computed. The numerical solution Φ_h is computed for various levels of uniform mesh refinements (as dictated by the maximum random access memory available). Each uniform refinement subdivides every triangle into four smaller ones. For structured meshes, the initial mesh T_h^0 consisted of two triangles, and about ten uniform refinements were usually carried out. For unstructured meshes, the initial mesh T_h^0 consisted of about 20 to 40 triangles, and about 6 to 8 uniform refinements were performed. We point out that the numerical solution and the reference (numerical) solutions are both obtained starting from the same initial mesh T_h^0. This common initial mesh allows for an easy implementation of the norm calculation, as each element in the uniformly refined or the adaptively refined mesh can be described by the refinement depth of an initial element in T_h^0. We now describe in more detail how the ele-ment integral appearing in the norm definition is computed. In the finite element framework, this integral can be written as

$$
\int_K d^3r (\Phi_h - \Phi_{ref})^2 = \int_K d^3r \, \Phi_h^2 - 2\int_K d^3r \, \Phi_{ref}\Phi_h
$$

$$
+ \int_K d^3r \, \Phi_{ref}^2
$$

$$
= \varphi^T M_{s(p)\times s(p)} \varphi
$$

$$
- 2 \sum_{i=1}^{4^{\ell(K)}} \varphi_{ref}^T M_{s(q)\times s(p)}^K P_{K\to K_i} \varphi
$$

$$
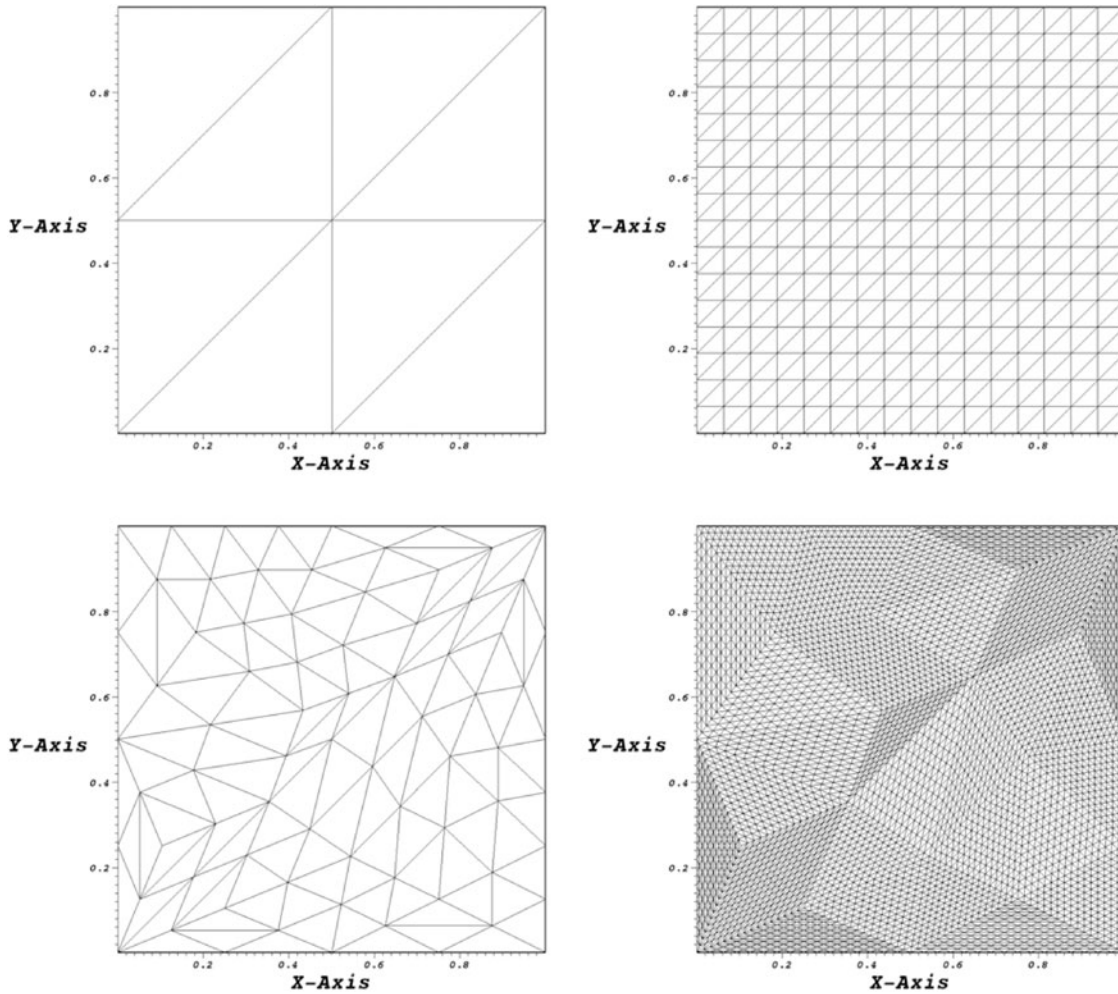+ \sum_{i=1}^{4^{\ell(K)}} \varphi_{ref}^T M_{s(q)\times s(q)}^{K_i} \varphi_{ref} \quad ,
$$

(14)

Fig. 2. Initial and three-time-refined meshes (left column: initial meshes; right column: three-time-refined meshes; structured meshes: top row; unstructured meshes: bottom row).

where

p = approximation order of the numerical solution ($p = 1, \ldots, 4$)

q = approximation order of the reference solution (again, we recall that we use $q = 4$)

$s(w) = (w + 1)(w + 2)/2$ = number of unknowns per triangle for an approximation of order w

$M_{s(w1) \times s(w2)}$ = rectangular mass matrix of size $s(w1) \times s(w2)$ and whose elements,

in terms of basis functions b, are given by

$$M^K_{s(q) \times s(p)}(i, j) = \int_K b_i(x, y) b_j(x, y) \, dx dy \;,$$

for $i = 1, \ldots, s(q)$ and $j = 1, \ldots, s(p)$ \hfill (15)

and the φ coefficients are the expansion coefficients of Φ in the finite element basis:

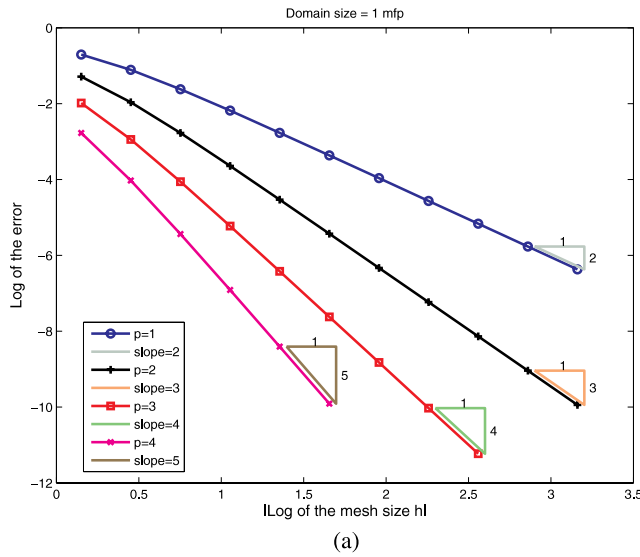$$\Phi(x, y) = \sum_{i=1}^{s(p)} \varphi^i b_i(x, y) \tag{16}$$
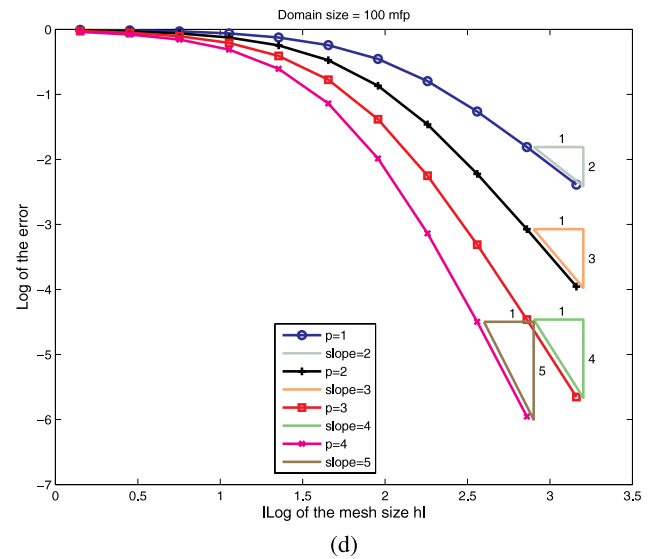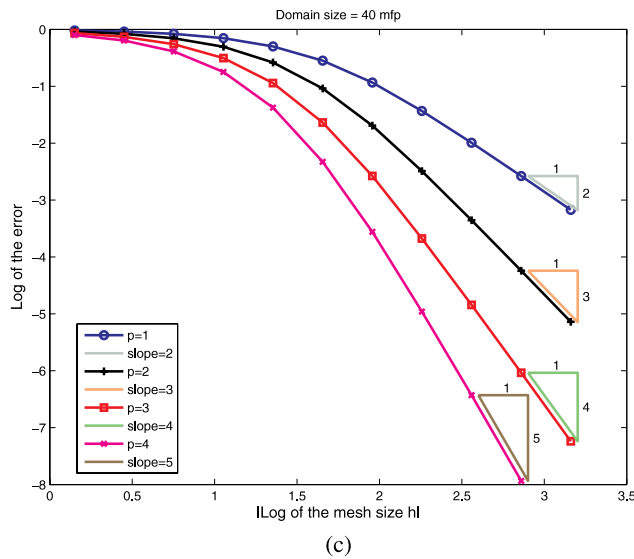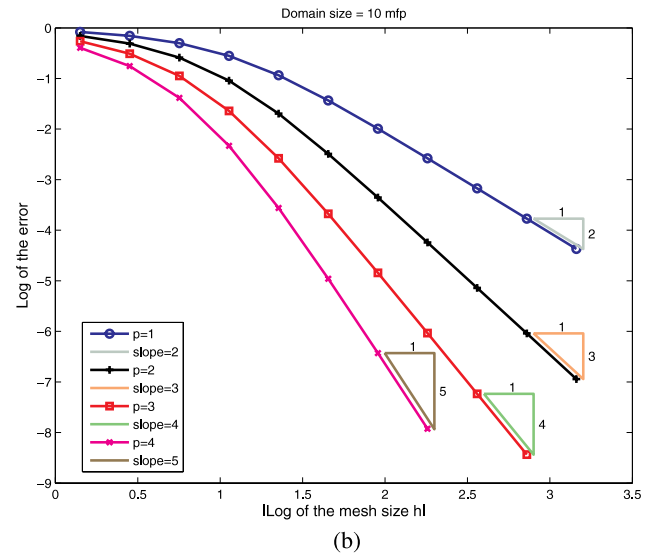
Fig. 3. Convergence rates: pure absorber case with 45-deg left-face incidence, structured mesh aligned with incident beam, domain size equal to (a) 1 mfp, (b) 10 mfp, (c) 40 mfp, and (d) 100 mfp.

and

$$\Phi_{ref}(x, y) = \sum_{i=1}^{s(q)} \varphi_{ref}^i b_i(x, y) \ . \tag{17}$$

The operator $P_{K \to Ki}$ restricts the values of Φ_h, defined on element K, to smaller elements K_i of the AMR mesh (the union of the AMR elements forms the element K: $\bigcup_{i=0}^{4^{\ell(K)}} Ki = K$). The quantity $\ell(K)$ appearing in the upper bound of the summation in Eq. (14) is the difference, in terms of mesh refinement levels, between the current element K in T_h (which was obtained by several successive uniform refinements of an element in T_h^0) and

the elements K_i in the adapted mesh T^{AMR}. For instance, at the third uniform refinement, a given element K_0 of the original mesh had been successively refined three times, and therefore, the element K on the current mesh is one of the $4^3 = 64$ children of that original element K_0. Likewise, during the AMR procedure, the same original element K_0 may have been refined, say, n times; thus, in this example, $\ell(K) = n - 3$. Obviously, it is possible that the uniform mesh refinement process leads to regions of the domain that are more refined than when using the AMR procedure. In this case, some elements of the AMR mesh can be coarser than elements of the uniformly refined mesh; hence $\ell(K) < 0$, and Eq. (14) needs to be replaced by
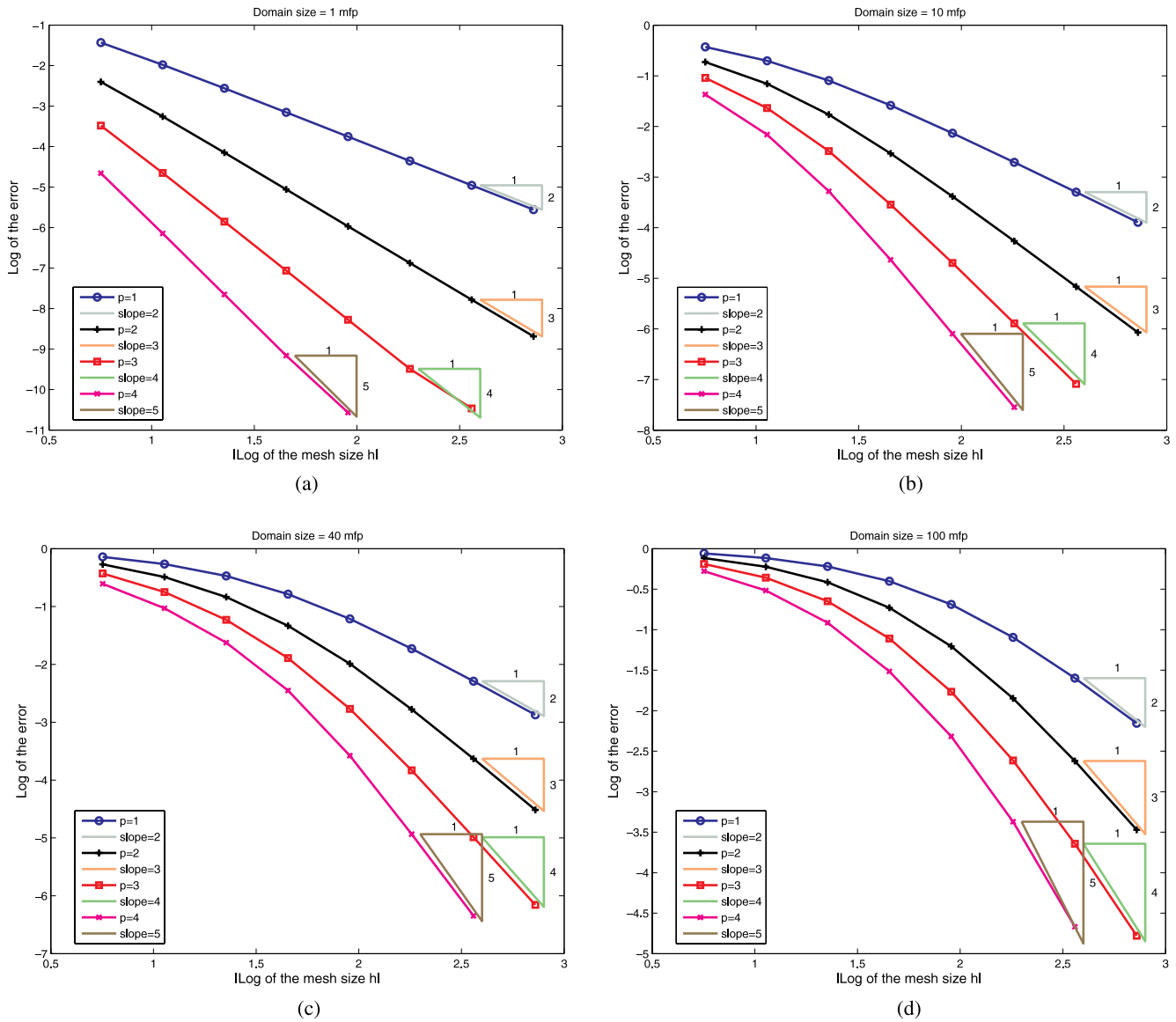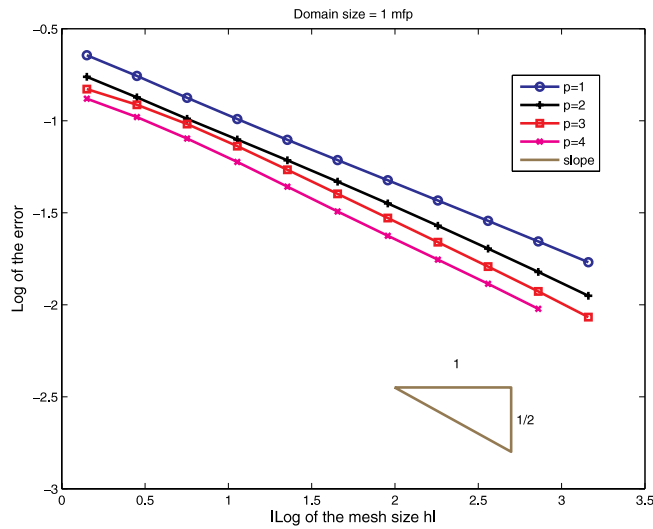

Fig. 4. Convergence rates: pure absorber case with 45-deg left-face incidence, unstructured mesh aligned with incident beam, domain size equal to (a) 1 mfp, (b) 10 mfp, (c) 40 mfp, and (d) 100 mfp.

$$\int_K d^3 r (\Phi_h - \Phi_{ref})^2$$

$$= \varphi M_{s(p) \times s(p)}^K \varphi - 2 P_{Ki \to K} \varphi_{ref} M_{s(q) \times s(p)}^K \varphi$$

$$+ P_{Ki \to K} \varphi_{ref} M_{s(q) \times s(q)}^K P_{Ki \to K} \varphi_{ref} \ , \qquad (18)$$

where the coarser AMR element K_i is restricted to the finer element K. Note that $P_{Ki \to K} = (P_{K \to Ki})^T$. Even though in this case the reference solution is computed on a coarser mesh, the AMR procedure identified this region of the domain as having little or no contribution to the error. Furthermore, we recall that the reference solution is obtained with the highest spatial approximation available:

$p = 4$. Therefore, we expect this should bear no consequences on the norm computations, as the results will later demonstrate. We give now a short example describing the mass and prolongation matrices, assuming, for simplicity, that both Φ_h and Φ_{ref} are linear finite element representations. The function Φ_h is given on element K, and the function Φ_{ref} is given on the element K once refined (i.e., on four triangles K_1 through K_4). In this case, the various matrices are
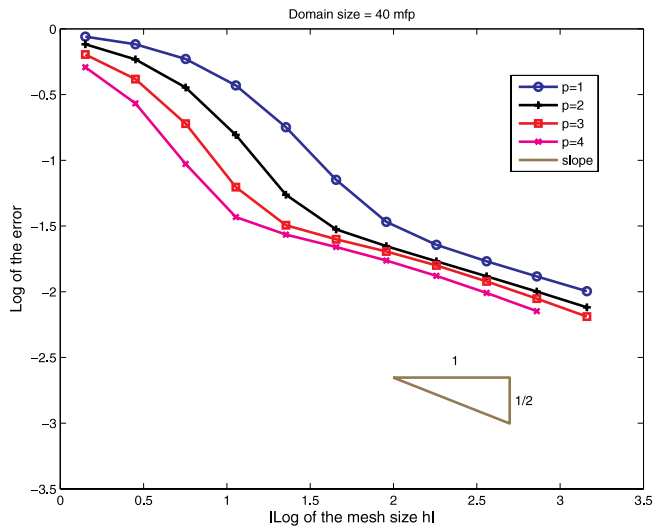
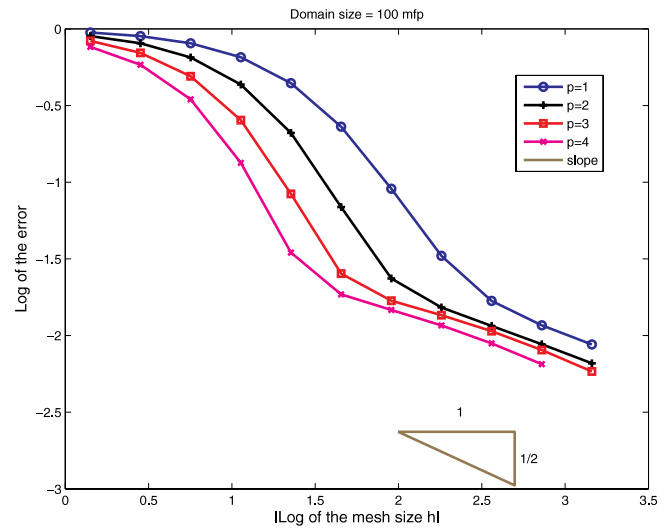$$M_{3,3}^K = \frac{Area(K)}{12} \begin{bmatrix} 2 & 1 & 1 \\ 1 & 2 & 1 \\ 1 & 1 & 2 \end{bmatrix} \ ,$$
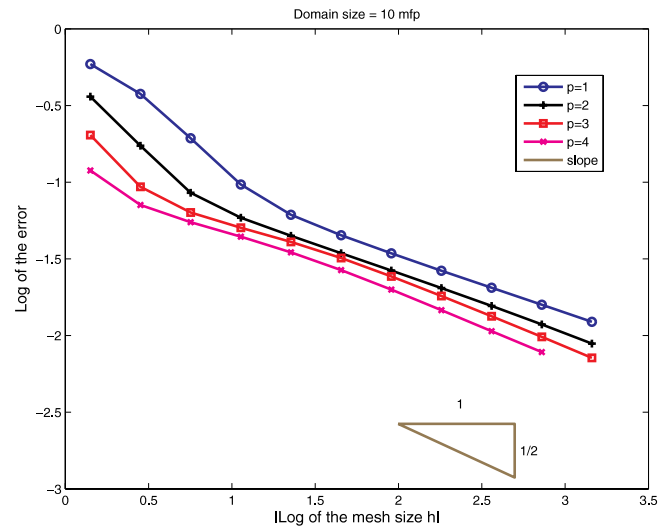
Fig. 5. Convergence rates: pure absorber case with ~18-deg left-face incidence, structured mesh not aligned with incident beam, domain size equal to (a) 1 mfp, (b) 10 mfp, (c) 40 mfp, and (d) 100 mfp.
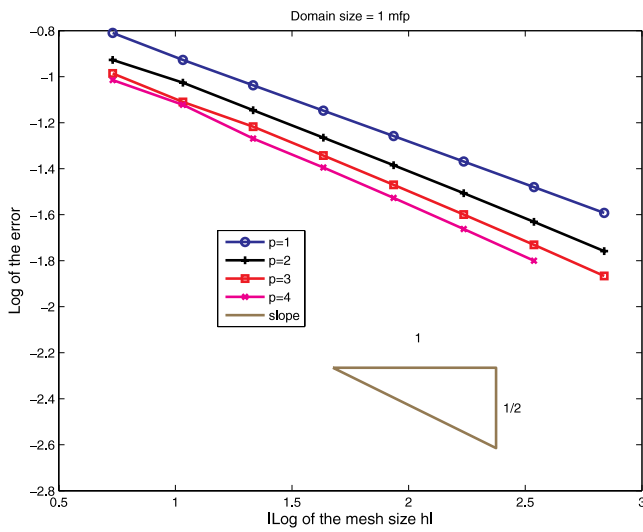
$$P_{K \to K_1} = \begin{bmatrix} 1 & 0 & 0 \\ \frac{1}{2} & \frac{1}{2} & 0 \\ \frac{1}{2} & 0 & \frac{1}{2} \end{bmatrix} \,, \qqua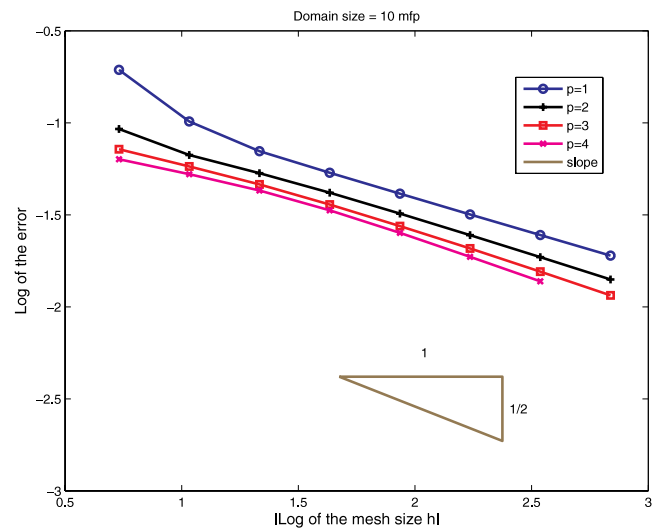d\qquad P_{K \to K_3} = \begin{bmatrix} \frac{1}{2} & 0 & \frac{1}{2} \\ 0 & \frac{1}{2} & \frac{1}{2} \\ 0 & 0 & 3 \end{bmatrix} \,,$$

$$P_{K \to K_2} = \begin{bmatrix} \frac{1}{2} & \frac{1}{2} & 0 \\ 0 & 1 & 0 \\ 0 & \frac{1}{2} & \frac{1}{2} \end{bmatrix} \,, \qquad\qquad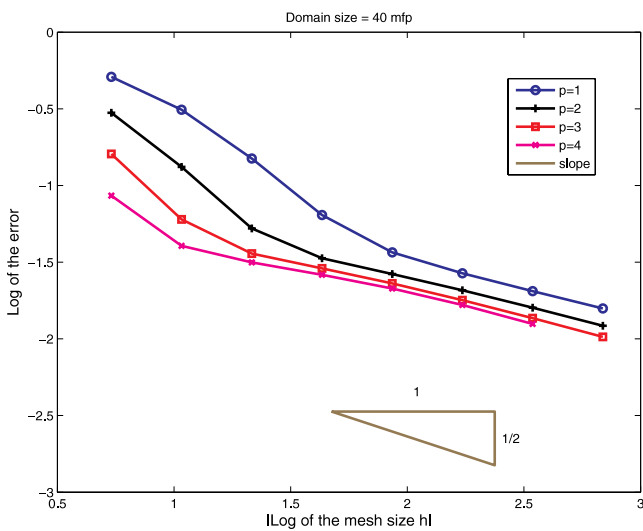 P_{K \to K_4} = \begin{bmatrix} 0 & \frac{1}{2} & \frac{1}{2} \\ \frac{1}{2} & 0 & \frac{1}{2} \\ \frac{1}{2} & \frac{1}{2} & 0 \end{bmatrix} \,,$$
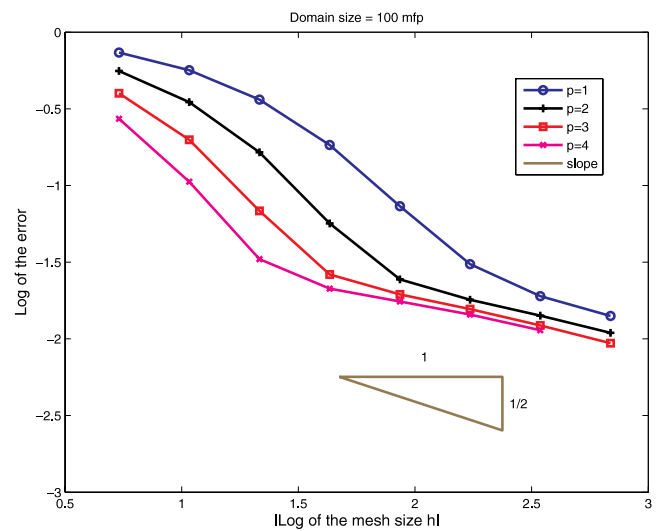

Fig. 6. Convergence rates: pure absorber case with ~18-deg left-face incidence, unstructured mesh not aligned with incident beam, domain size equal to (a) 1 mfp, (b) 10 mfp, (c) 40 mfp, and (d) 100 mfp.

and

$$\int_K d^3r (\Phi_h - \Phi_{ref})^2$$

$$= \varphi M_{3,3}^K \varphi + 2 \sum_{i=1}^4 \left[\varphi_{ref} M_{3,3}^{Ki} P_{K \to K_i} \varphi \right.$$

$$\left. + \varphi_{ref} M_{3,3}^{Ki} \varphi_{ref} \right] . \quad (19)$$

V. RESULTS

Convergence results are presented in this section. These test cases are inspired by Larsen's[7] and Azmy's[9] work. A square domain containing a homogeneous material is modeled. The total cross section σ_t is 1 cm^{-1}. We considered the cases of a pure absorber ($\sigma_{s,0} = 0$ cm^{-1}) and a scattering medium ($\sigma_{s,0} = 0.5$ cm^{-1}). Seven different square widths W were employed: 1, 5, 10, 20, 40, 60, and 100 cm, resulting in optical thicknesses ranging from 1 to 100 mean free paths (mfp). No volumetric external sources are present. Spatially uniform incident beam fluxes are applied either on the left face [$\Psi^{inc}(x = 0, y) = 1$] or on both left and bottom [$\Psi^{inc}(x = 0, y) = \Psi^{inc}(x, y = 0) = 1$] faces simultaneously. We considered two incident directions: a direction with exactly a 45-deg angle with respect to the axes and another direction with an angle of ~ 18.444 deg with respect to the x-axis

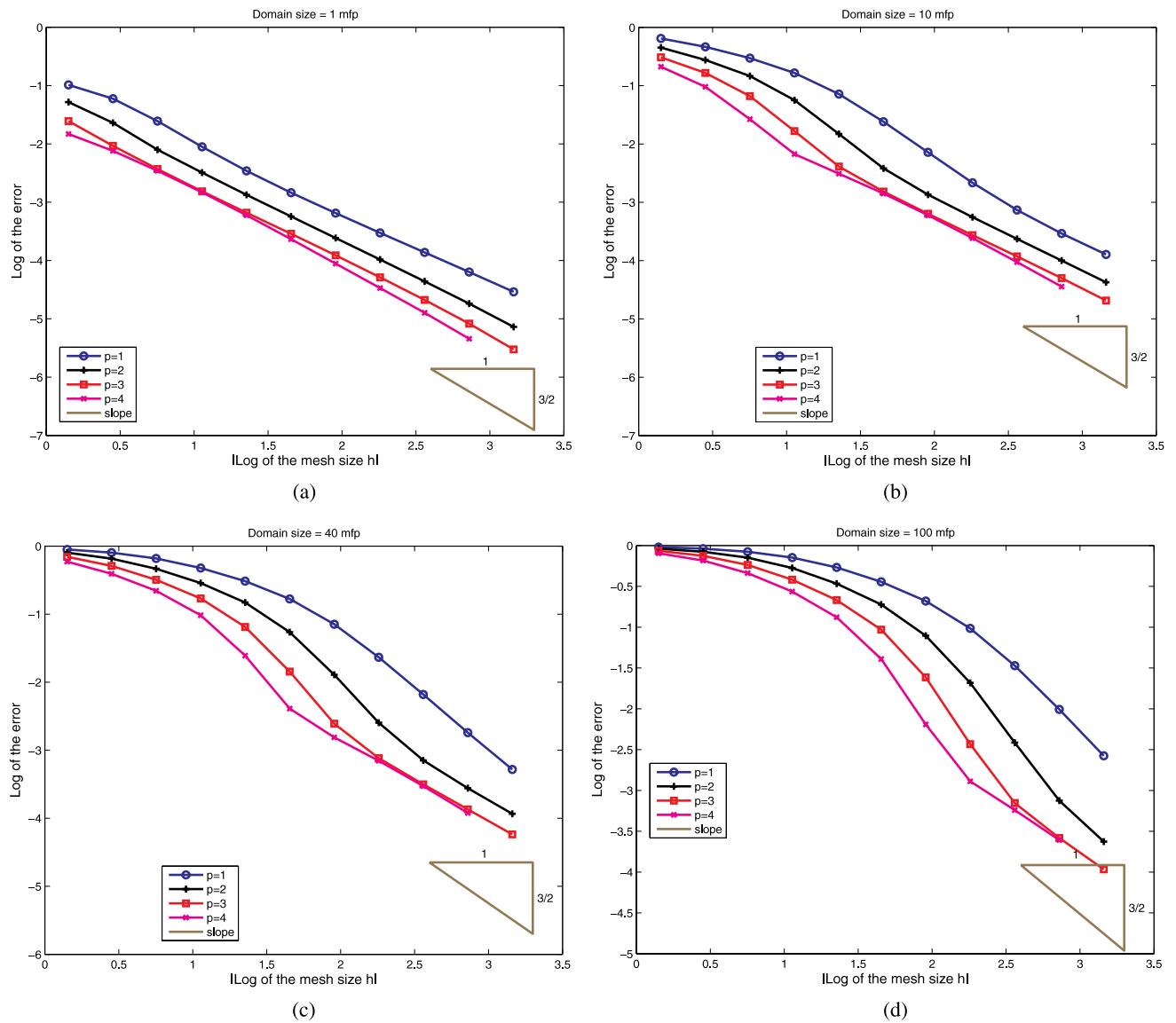
Fig. 7. Convergence rates: pure absorber case with $\sim$18-deg (left + bottom)-face incidence, structured mesh not aligned with incident beam, domain size equal to (a) 1 mfp, (b) 10 mfp, (c) 40 mfp, and (d) 100 mfp.

(an S_4 angular quadrature is used in these tests; its directions form angles of $18.444\ldots,45$, and $71.556\ldots$ deg with respect to the x-axis in the first quadrant). The use of a 45-deg angle in a square domain makes it particularly easy to align the mesh with the singularity (incident beam direction stemming from the domain corner). The use of the other direction ($\sim 18.444\ldots$ deg) serves as a test case in which the mesh is not aligned with the incident boundary fluxes. When the flux is incident only on the left face, we should expect a more abrupt transition across the characteristic line separating the illuminated portion of the domain from the nonilluminated one (the flux is discontinuous in the case of a pure absorber). For an incoming flux, of equal value, incident on both the left and bottom faces, the flux inside the domain will present fewer singularities (in this case, the flux is indeed continuous inside the domain, even for a pure absorber medium).

We propose to analyze the effect of singularities in the transport solution on DGFEM(p) for (a) fluxes incident on one or two adjacent faces, (b) with meshes aligned or not with the incident direction, (c) for materials with or without scattering, (d) in configurations of various optical thicknesses, and (e) on sequences of uniformly refined structured and unstructured meshes. Convergence results and some discussions are provided for these various cases. The initial structured and unstructured meshes are given in Fig. 2 (left panes). After three uniform refinements, the meshes are graphed in Fig. 2 (right panes). We have chosen to uniformly refine the original meshes, rather than regenerate new meshes with a smaller triangle area constraint in order to be able to compute the norms as indicated in Sec. IV.B, where we required that all refined meshes be subdivisions of the same initial mesh. As we will see from the results, having grids with triangles of various sizes does not affect the convergence rates.

V.A. Flux Incident on the Left Face, Pure Absorber Case

A left incident beam is applied on the domain geometry. The transport solution in the domain is singular (with discontinuity) along the characteristic line emanating from the bottom-left corner in the direction of the incident particles. Mathematically, the transport solution is in the $H^{1/2-\varepsilon}(D)$ space.

For a 45-deg incident flux, the meshes employed are perfectly aligned with the discontinuity of the transport solution. The convergence rates for DGFEM(1) through DGFEM(4), measured in the L_2 norm, are plotted in Fig. 3 (structured meshes aligned with the 45-deg singularity) and Fig. 4 (unstructured meshes aligned with the 45-deg singularity). The plots are provided for domains of optical thicknesses of 1, 10, 40, and 100 mfp. We can clearly see that the DGFEM(p) method is converging at the theoretical rate of $p + 1$. In this

case where the mesh is aligned with the singularity, the DGFEM "does not see" the lack of regularity of the solution.

We repeated these calculations, but this time, we employed an $\sim$18-deg incident beam (i.e., the meshes are not aligned with the transport solution singularity). Figure 5 provides the convergence rates for the structured grids (domain thicknesses of 1, 10, 40, and 100 mfp), and Fig. 6 gives the convergence rates for the unstructured grids (domain thicknesses of 1, 10, 40, and 100 mfp). We note that for optically thin domains (and thus optically thin meshes), the convergence rate is dictated by the regularity of the transport solution; i.e., all convergence slopes are equal to $\frac{1}{2}$. For thicker domains, higher convergence rates are observed as long as the mesh width remains greater than the mfp. In this case, we observe a preasymptotic region where the convergence rates tend to the higher theoretical value of $p + 1$ without quite attaining that value. When mesh widths become optically thin, the regularity of the solution once again limits the convergence to a slope of $\frac{1}{2}$.

We also note that in any case, the error is always lower for higher polynomial orders. Thus, even if no enhanced convergence rates are observed, it may still be advantageous to use higher-order polynomials in order to have smaller error values.

V.B. Flux Incident on Both the Left and Bottom Faces, Pure Absorber Case

Two incident beams, of identical direction and intensity, are now applied to both the left and bottom faces. In this case, the transport solution is continuous inside the
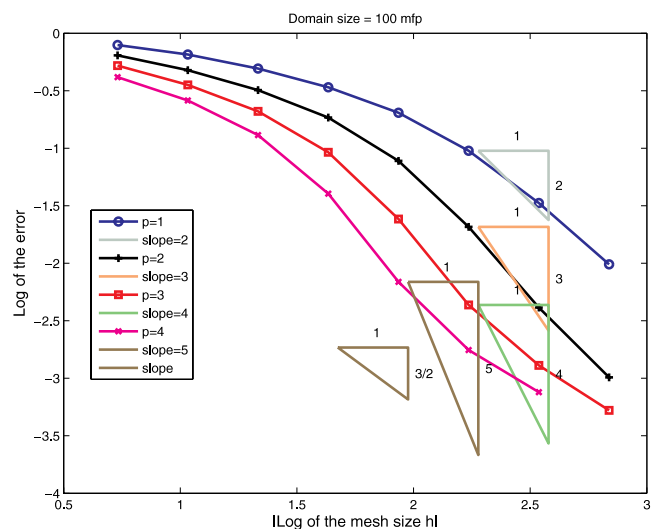

Fig. 8. Convergence rates: pure absorber case with $\sim$18-deg (left + bottom)-face incidence, unstructured mesh not aligned with incident beam, domain size equal to 100 mfp.

domain and belongs to the $H^{3/2-\varepsilon}(D)$ space. When using a 45-deg incident beam (i.e., grids are aligned with the singularity), we recover results identical to the above one-beam case (Sec. V.A), when meshes were aligned with the discontinuity. For brevity, we do not show any convergence plots for the case with alignment of this section but only state the conclusions: Regardless of the domain or mesh optical thickness, the DGFEM(p) converges at a rate of $p+1$ measured in the standard L_2 norm, with lower errors as the polynomial order is increased.

In the case of an $\sim$18-deg incident beam, the meshes are no longer aligned with the singularity of the transport solution, but because of the higher regularity of the transport solution (which is now continuous), a conver-

gence rate of $\frac{3}{2}$ is achieved. As noted previously, for optically thick meshes (coarser meshes), the convergence rate is higher than the $\frac{3}{2}$ value imposed by the solution regularity and is dependent upon p; for $p = 1, 2, 3$, the convergence rates observed tend to the value of $p + 1$; for $p = 4$, the regularity of the solution prevented the rate to fully reach a value of 5. As the meshes are refined, the convergence rates tend toward the asymptotic limit of $\frac{3}{2}$, regardless of the polynomial bases used. Figure 7 gives the convergence rates for the structured grids (domain thicknesses of 1, 10, 40, and 100 mfp). Figure 8 shows the rates for the unstructured grid for a domain of 100 mfp thick, and rates almost equal to $p + 1$ are observed for intermediate mesh sizes.
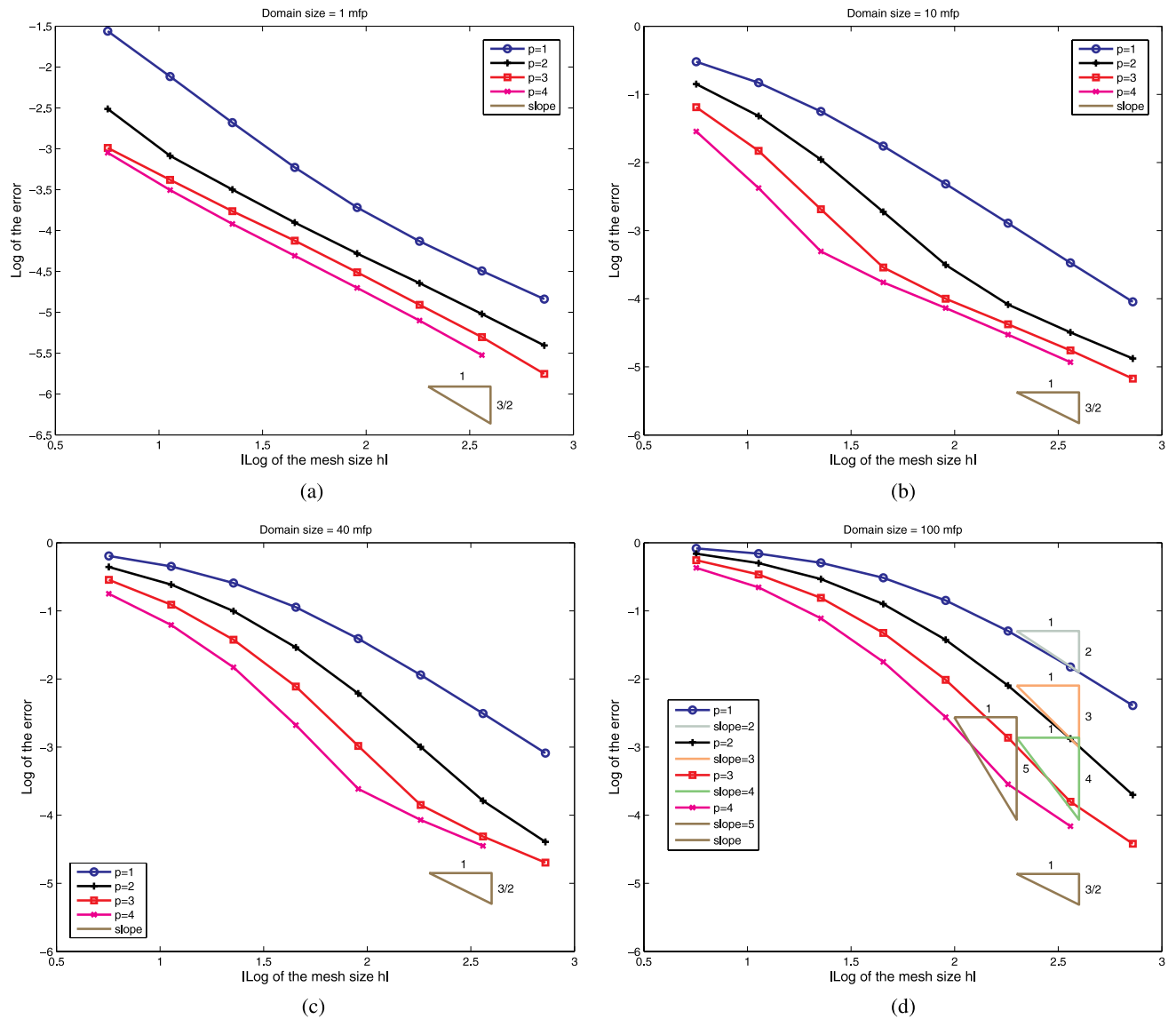

Fig. 9. Convergence rates: scatterer case with 45-deg left-face incidence, unstructured mesh aligned with incident beam, domain size equal to (a) 1 mfp, (b) 10 mfp, (c) 40 mfp, and (d) 100 mfp.

V.C. Flux Incident on the Left Face, Scatterer Material Case

In the case of a scatterer material, it is well known that the S_N transport solution will present singularities originating from the corners of the domain in each discrete ordinates direction.[29] It is of great practical interest to investigate how DGFEM(p) converges in this case, as many applications include scattering. We once again used the above-mentioned S_4 quadrature.

In this first series of tests, the incident beam is aligned along the 45-deg direction. When meshes are aligned with the incident particles, convergence rates obtained ranged from (a) a polynomial-order–dependent value (close to but less than $p + 1$) for optically thick meshes (in the preasymptotic range) to (b) $\frac{3}{2}$ for optically thin meshes. Again, it is not unexpected to fall short of the $p + 1$ rate for coarse cells, as the theoretical results hold in the asymptotic limit (i.e., as the mesh size tends toward 0). Here, in the asymptotic region, the rate is limited by the regularity of the solution, and the rates graphed in Fig. 9 show the transitions from the higher-order convergence rate region (coarser meshes) to a convergence rate of $\frac{3}{2}$ (finer/optically thin meshes). These figures are for unstructured meshes. Similar results, not presented here for brevity, were obtained for structured meshes. In Fig. 9d (domain size = 100 mfp), the asymptotic slope of $\frac{3}{2}$ and the preasymptotic slopes of $p + 1$ are shown.
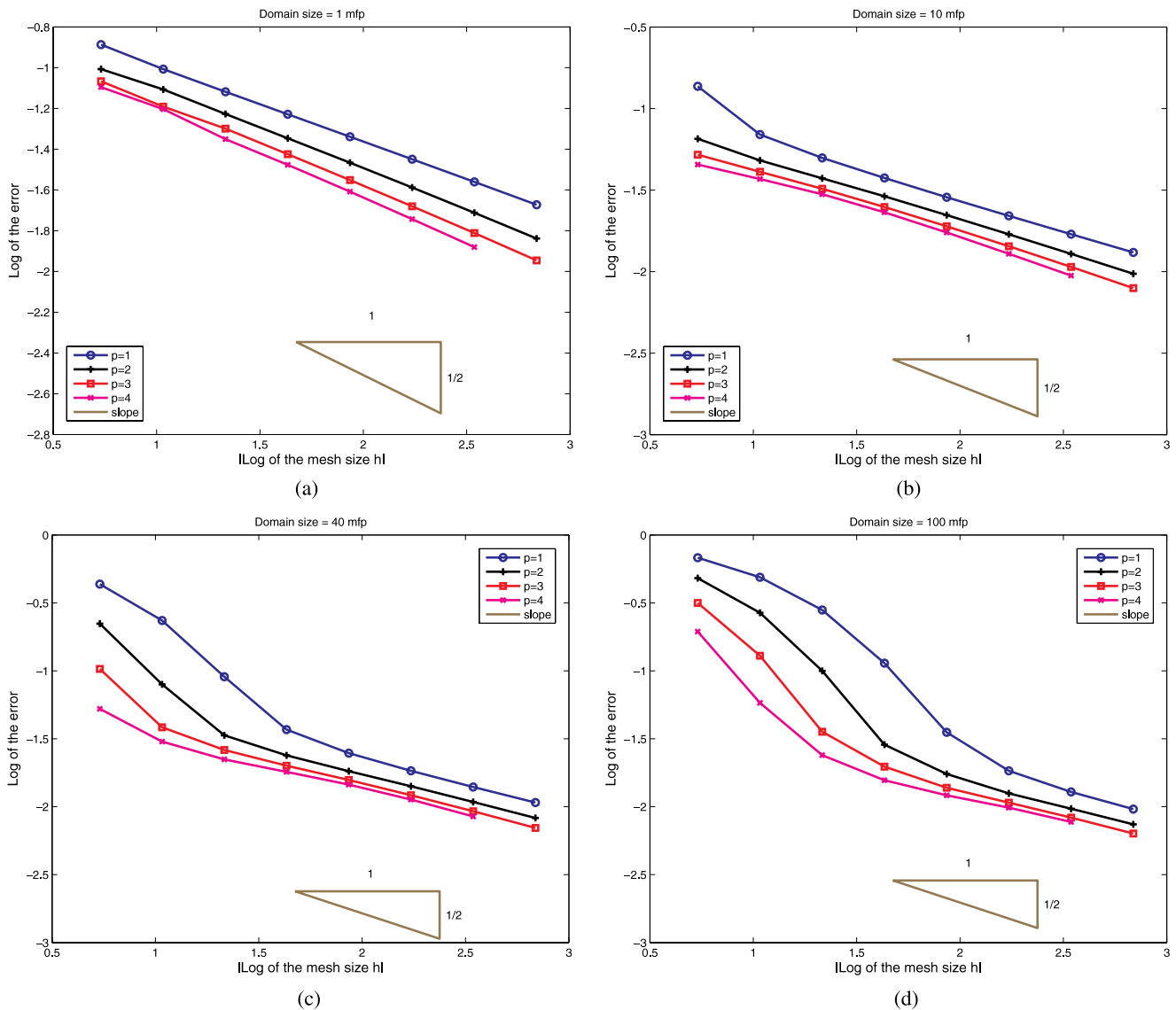

Fig. 10. Convergence rates: scatterer case with $\sim$18-deg left-face incidence, unstructured mesh not aligned with incident beam, domain size equal to (a) 1 mfp, (b) 10 mfp, (c) 40 mfp, and (d) 100 mfp.
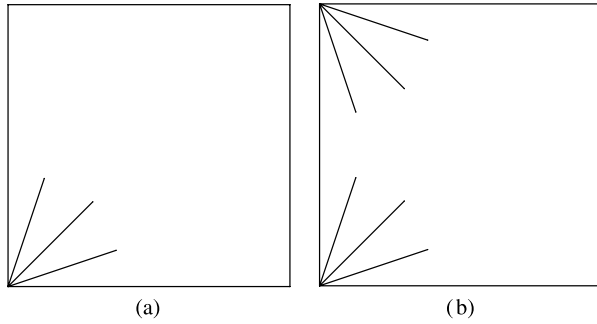
Fig. 11. Meshes partially aligned with singularities: (a) singularities of the bottom-left corner only and (b) singularities of the bottom-left and top-left corners.

For a beam incident at an angle of ~18 deg, we again have the case where the meshes are not aligned with the singularity of the transport solution. The observed convergence rates varied from a polynomial-order–dependent high value to a regularity imposed rate of $\frac{1}{2}$ (see Fig. 10).

V.D. Flux Incident on the Left Face, Scatterer Material Case with Partial Mesh Alignment

The requirement of having a mesh fully aligned with the singularities may seem a severe obstacle in general and for AMR in particular. Recognizing that mesh adaptation has been successfully applied in other engineering fields with hyperbolic equations (Ref. 30), we propose a
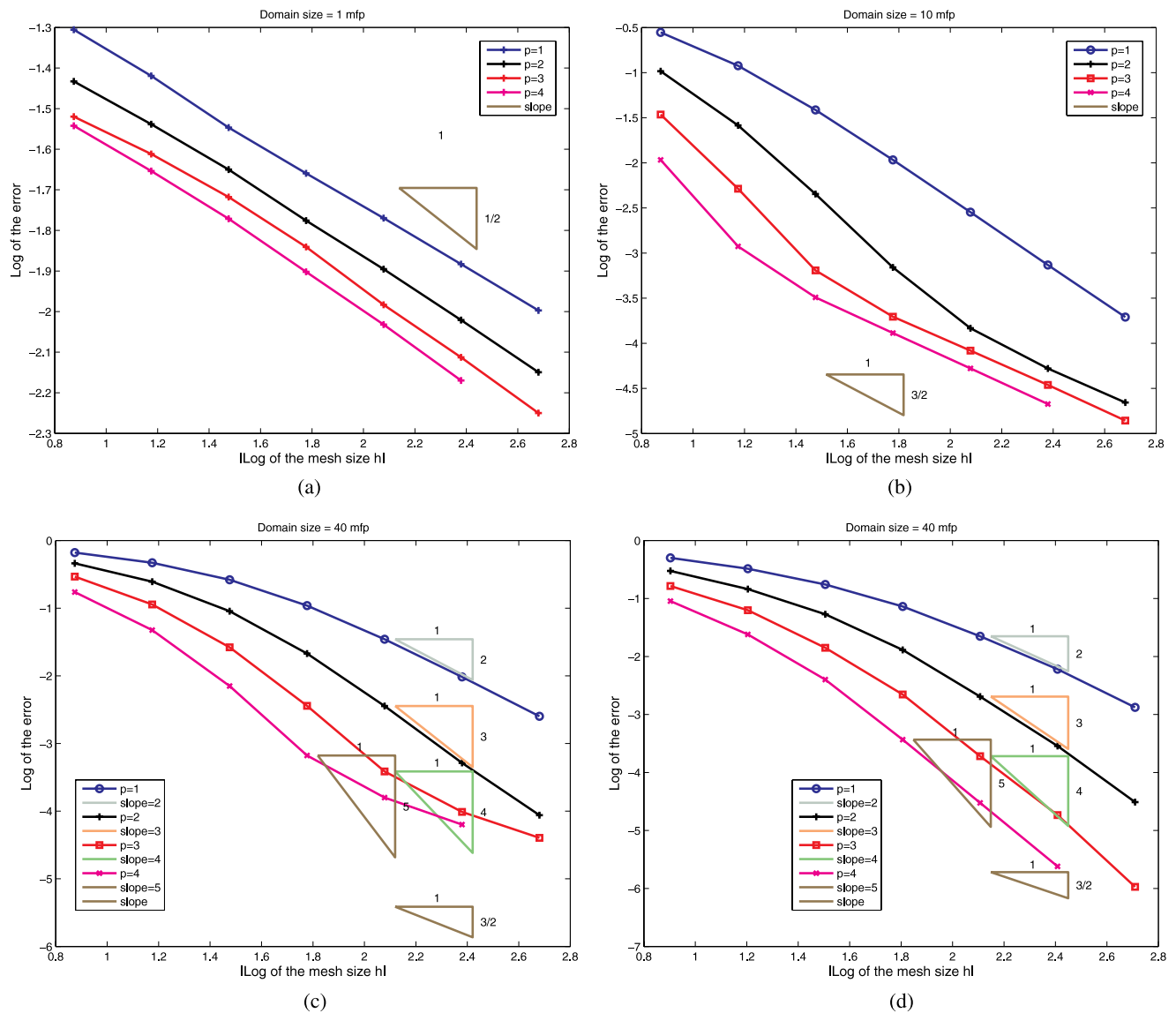

Fig. 12. Convergence rates: scatterer case with ~18-deg left-face incidence, mesh partially aligned with singularities at the lower-left corner, domain size equal to (a) 1 mfp, (b) 10 mfp, (c) 40 mfp; (d) singularities at both the bottom-left and upper-left corners.

simple test, where the domain contains meshes that are partially aligned with the singularity (Fig. 11). We use the scatterer test case of Sec. V.C, where the asymptotic convergence rate is $\frac{3}{2}$ for meshes fully aligned with the singularity and $\frac{1}{2}$ for unaligned meshes (see Figs. 9 and 10). In Sec. V.C, we have also noted that before reaching their asymptotic rates, rates close to $p + 1$ can be attained. We now compare these previous results with the results obtained with partially aligned meshes and shown in Fig. 11. In Fig. 11a, the mesh is aligned with the three singularities (one per ordinate) present at the lower-left corner. In Fig. 11b, the mesh is also aligned with the three singularities present at the upper-left corner. For conciseness, we show only the mesh that is the input data for the triangle mesh generator. We also generated meshes partially aligned with the singularities of all four corners.

We first carried out tests where singularities are partially meshed for the bottom-left corner only. For very thin domains, rates of $\frac{1}{2}$ are reached; the mesh alignment is too short (optically thin domain) to recover a higher convergence rate. Nonetheless, the errors obtained with the partially aligned meshes are smaller by a factor of 3 to 5 compared with the case where the mesh is not aligned with the singularity (see Fig. 12). For domains >10 mfp (see Figs. 12b and 12c), the asymptotic rate is now $\frac{3}{2}$, which is a vast improvement over the $\frac{1}{2}$ rate for unaligned meshes. The magnitude of the error has also been further decreased by two orders of magnitude, in comparison with the unaligned case.

When tests were repeated in which the singularities were partially meshed for both lower-left and upper-left corners, the observed asymptotic rates for thin domains were $\frac{3}{2}$ (as compared to $\frac{1}{2}$ previously). Thus, taking into account singularities from both corners allowed us to recover the maximum regularity-constrained theoretical rate. For thicker domains (>20 mfp), the partial meshing of the singularities is enough to recover convergence rates of $p + 1$; i.e., the results are no longer constrained by the solution regularity. We present the results for a 40-mfp-thick domain. The accuracy gains range from ~0.5 ($p = 1$) to almost 2 ($p = 4$) orders of magnitude (see Fig. 12d). This is particularly noteworthy when considering the potential for adaptive mesh computations in transport. As we have seen in our tests, even if aligning the mesh was not always sufficient to augment the convergence rate, the magnitude of the error always decreased significantly. At that stage, and by surveying current practice in other disciplines, we can conjecture that accuracy gains can be obtained by resolving, albeit partially, the singularity in the transport equation.

V.E. Discontinuous Galerkin Norm Computations

We recalled in Sec. III that the error, measured in the DG norm, converges at a rate that is reduced by $\frac{1}{2}$ in comparison to the L_2 norm. We briefly provide numerical results that corroborate these theoretical facts. First, in Fig. 13, we show the rates in the case of a pure absorber where the mesh is aligned with the singularity (domain size = 10 mfp, Fig. 13a). In the L_2 norm, rates were of $p + 1$ (see previous results); now, we clearly observed rates of $p + \frac{1}{2}$. Then, we tested a pure absorber case, where the mesh does not align with the singularity (domain size = 100 mfp, Fig. 13b). In this situation, the theoretical value of the error in the DG norm is 0, which can be noted in Fig. 13b.
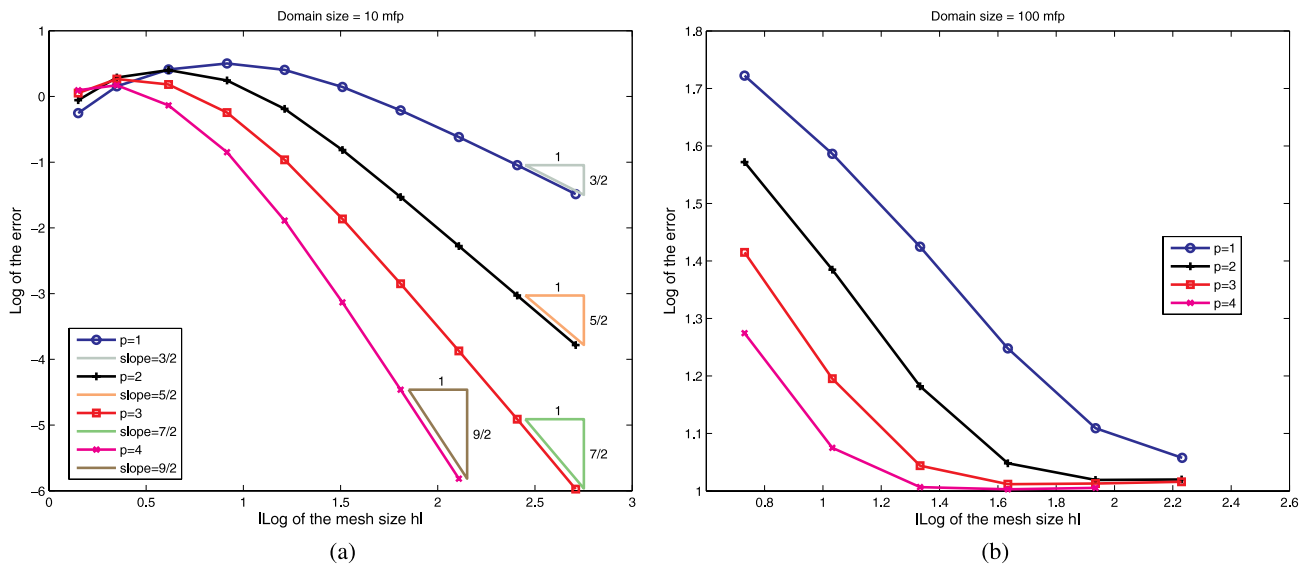

Fig. 13. Convergence rates in the DG norm: pure absorber case with 45-deg left-face incidence, aligned with incident beam. (a) Domain size equal to 10 mfp, structured mesh and (b) domain size equal to 100 mfp, unstructured mesh.

VI. CONCLUSIONS

We have numerically analyzed the convergence properties of DG finite elements, up to polynomial order 4, for the spatial discretization of the transport equation. Test cases were carried out with pure absorber media and scatterer media, for structured and unstructured triangular meshes. We have verified theoretical convergence results; namely, that in the L_2 norm, the solutions converge with a rate of $\min(p+1, r)$, where p is the spatial approximation order and r is the transport solution regularity. In the DG norm, the theoretical rate of $\min(p+\frac{1}{2}, r-\frac{1}{2})$ was recovered. For optically thin meshes, the convergence rate in the L_2 norm is always imposed by the solution regularity ($r = \frac{1}{2}$ or $\frac{3}{2}$), but for thicker meshes, rates approaching $p+1$ are observed. We note that for optically thick domains, the error is significantly reduced by the convergence rate in $p+1$ before being limited by regularity for very fine meshes. In the cases where the meshes are partially aligned with a few singularities, convergence rates of $\frac{3}{2}$ (as opposed to $\frac{1}{2}$) can be attained. When more singularities are properly meshed, convergence at the rate of $p+1$ can be observed.

REFERENCES

1. N. K. MADSEN, "Convergence of Singular Difference Approximations for the Discrete Ordinate Equations in *x*-*y* Geometry," *Math. Comput.*, **26**, *117*, 45 (Jan. 1972).

2. N. K. MADSEN, "Convergent Centered Difference Schemes for the Discrete Ordinate Neutron Transport Equations," *SIAM J. Numer. Anal.*, **12**, *2*, 164 (Apr. 1975).

3. K. D. LATHROP, "Spatial Differencing of the Transport Equation: Positivity vs. Accuracy," *J. Comput. Phys.*, **4**, 475 (1969).

4. E. M. GELBART, J. A. DAVIS, and L. A. HAGEMAN, "Solution of the Discrete Ordinate Equations in One and Two Dimensions," *Proc. SIAM-AMS Mtg. Transport Theory*, Providence, Rhode Island, 1969, Vol. 1, p. 129, R. BELLMAN, G. BIRCKHOFF, and I. ABU-SHUMAYS, Eds., Society for Industrial and Applied Mathematics–American Mathematical Society (1969).

5. W. H. REED, "New Difference Equations for the Neutron Transport Equation," *Nucl. Sci. Eng.*, **46**, 309 (1971).

6. J. ARKUSZEWSKI, T. KULIKOWSKA, and J. MIKA, "Effects of Singularities on Approximation in S_N Methods," *Nucl. Sci. Eng.*, **49**, 20 (1972).

7. E. W. LARSEN, "Spatial Convergence Properties of the Diamond Difference Method in *x*, *y* Geometry," *Nucl. Sci. Eng.*, **80**, 710 (1982).

8. E. W. LARSEN and W. F. MILLER, Jr., "Convergence Rates of Spatial Difference Equations for the Discrete-Ordinates Neutron Transport Equations in Slab Geometry," *Nucl. Sci. Eng.*, **73**, 76 (1980).

9. J. I. DUO and Y. Y. AZMY, "Error Comparison of Diamond Difference, Nodal, and Characteristic Methods for Solving Multidimensional Transport Problems with the Discrete Ordinates Approximation," *Nucl. Sci. Eng.*, **156**, 139 (2007).

10. T. A. WAREING, J. M. McGHEE, J. E. MOREL, and S. D. PAUTZ, "Discontinuous Finite Element S_N Methods on Three-Dimensional Unstructured Grids," *Nucl. Sci. Eng.*, **138**, 256 (2001).

11. J. E. MOREL and J. S. WARSA, "An S_n Spatial Discretization Scheme for Tetrahedral Meshes," *Nucl. Sci. Eng.*, **151**, 157 (2005).

12. J. RAGUSA and Y. WANG, "A High-Order Discontinuous Galerkin Method for the S_N Transport Equations on 2D Unstructured Triangular Meshes," *Ann. Nucl. Eng.*, **36**, 931 (2009).

13. Y. WANG, J. C. RAGUSA, and M. DeHART, "An Unstructured Triangular Mesh Linear Discontinuous Solver for NEWT," *Proc. Int. Conf. Physics of Reactors, Nuclear Power: A Sustainable Resource (PHYSOR 2008)*, Interlaken, Switzerland, September 14–19, 2008.

14. "Discontinuous Galerkin Methods: Theory, Computation and Applications," *Lecture Notes in Computational Science and Engineering*, Vol. 11, B. COCKBURN, G. KARNIADAKIS, and C. SHU, Eds., Springer-Verlag, New York (2000).

15. G. E. KARNIADAKIS and S. J. SHERWIN, *Spectral/hp Element Methods for Computational Fluid Dynamics*, 2nd ed., Oxford University Press, New York (2005).

16. J. S. HESTHAVEN and T. WARBURTON, *Nodal Discontinuous Galerkin Methods: Algorithms, Analysis, and Applications*, Springer, New York (2007).

17. P. SOLIN, *Partial Differential Equations and the Finite Element Method*, John Wiley and Sons, New York (2005).

18. W. H. REED and T. R. HILL, "Triangular Mesh Methods for Neutron Transport Equation," LA-UR-73-479, Los Alamos Scientific Laboratory (1973).

19. W. H. REED, T. R. HILL, F. W. BRINKLEY, and K. D. LATHROP, "TRIPLET: A Two-Dimensional, Multigroup Triangular, Planar Geometry, Explicit Transport Code," LA-5428-MS, Los Alamos Scientific Laboratory (1973).

20. P. LESAINT and P. A. RAVIART, "On a Finite Element Method for Solving the Neutron Transport Equation," *Mathematical Aspects of Finite Elements in Partial Differential Equations*, p. 89, C. A. DE BOOR, Ed., Academic Press, New York (1974).

21. E. E. LEWIS and W. F. MILLER, Jr., "Computational Methods of Neutron Transport," John Wiley and Sons, New York (1984).

22. J. R. SHEWCHUK, "Triangle: Engineering a 2D Quality Mesh Generator and Delaunay Triangulator," *Applied Computational Geometry: Towards Geometric Engineering*, *Lecture Notes in Computer Science*, Vol. 1148, p. 203, M. C. LIN and D. MANOCHA, Eds., Springer-Verlag, Berlin, Germany (May 1996).

23. C. JOHNSON and J. PITKARANTA, "Convergence of a Fully Discrete Scheme for Two-Dimensional Neutron Transport," *SIAM J. Numer. Anal.*, **20**, *5*, 951 (Oct. 1983).

24. T. E. PETERSON, "A Note on the Convergence of the Discontinuous Galerkin Method for a Scalar Hyperbolic Equation," *SIAM J. Numer. Anal.*, **28**, *1*, 133 (Feb. 1991).

25. G. R. RICHTER, "An Optimal-Order Error Estimate for the Discontinuous Galerkin Method," *Math. Comput.*, **50**, *181*, 75 (Jan. 1988).

26. J-L LIONS and E. MAGENES, "Problèmes aux limites non homogènes et applications," Chapter 9, Dunod, Paris, France (1968).

27. P. HOUSTON, C. SCHWAB, and E. SULI, "Stabilized hp-Finite Element Methods for First-Order Hyperbolic Problems," *SIAM J. Numer. Anal.*, **37**, *5*, 1618 (2000).

28. P. HOUSTON, C. SCHWAB, and E. SULI, "Discontinuous hp-Finite Element Methods for Advection-Diffusion-Reaction Problems," *SIAM J. Numer. Anal.*, **39**, *6*, 2133 (2002).

29. R. B. KELLOGG, "Numerical Analysis of the Neutron Transport Equations," *Numerical Solution of Partial Differential Equations—III, SYNSPADE 1975*, B. HUBBARD, Ed., Academic Press, New York (1976).

30. M. J. BERGER and P. COLELLA, "Local Adaptive Mesh Refinement for Shock Hydrodynamics," *J. Comput. Phys.*, **82**, *1*, 64 (May 1989).